

Analyzing the Hubble tension through hidden sector dynamics in the early universe

Amin Aboubrahim,^a Michael Klasen^a and Pran Nath^b

^aInstitut für Theoretische Physik, Westfälische Wilhelms-Universität Münster, Wilhelm-Klemm-Straße 9, Münster 48149, Germany

^bDepartment of Physics, Northeastern University,111 Forsyth Street, Boston, MA 02115-5000, U.S.A.

E-mail: aabouibr@uni-muenster.de, michael.klasen@uni-muenster.de, p.nath@northeastern.edu

Received February 10, 2022 Revised March 21, 2022 Accepted March 30, 2022 Published April 21, 2022

Abstract. The recent analysis from the SH0ES collaboration has confirmed the existence of a Hubble tension between measurements at high redshift (z > 1000) and at low redshift (z < 1) at the 5σ level with the low redshift measurement giving a higher value. In this work we propose a particle physics model that can help alleviate the Hubble tension via an out-of-equilibrium hidden sector coupled to the visible sector. The particles that populate the dark sector consist of a dark fermion, which acts as dark matter, a dark photon, a massive scalar and a massless pseudo-scalar. Assuming no initial population of particles in the dark sector, feeble couplings between the visible and the hidden sectors via kinetic mixing populate the dark sector even though the number densities of hidden sector particles never reach their equilibrium distribution and the two sectors remain at different temperatures. A cosmologically consistent analysis is presented where a correlated evolution of the visible and the hidden sectors with coupled Boltzmann equations involving two temperatures, one for the visible sector and the other for the hidden sector, is carried out. The relic density of the dark matter constituted of dark fermions is computed in this two-temperature formalism. As a consequence, BBN predictions are upheld with a minimal contribution to $\Delta N_{\rm eff}$. However, the out-of-equilibrium decay of the massive scalar to the massless pseudo-scalar close to the recombination time causes an increase in $\Delta N_{\rm eff}$ that can help weaken the Hubble tension.

Keywords: particle physics - cosmology connection, cosmology of theories beyond the SM, dark matter theory

ArXiv ePrint: 2202.04453

Co	ontents	
1	Introduction	1
2	The model	3
3	Evolution of hidden and visible sector temperatures	5
4	Departure from kinetic equilibrium	7
5	Numerical analysis: yield and temperature evolution prior to decoupling	8
6	Contributions to $\Delta N_{ ext{eff}}$	12
7	Reheating of the dark sector bath prior to recombination	14
8	Conclusion	16
9	Further details of the analysis	17
A	Degrees of freedom	17
В	Model details	18
\mathbf{C}	Boltzmann equations with visible and hidden sector temperatures	18

1 Introduction

Recently the SH0ES collaboration [1] has confirmed at 5σ level the tension between measurements of the Hubble parameter H_0 at high redshift (z > 1000) and at low redshift (z < 1). Based on the Lambda-cold dark matter (Λ CDM) model and an analysis of data from the times of Big Bang Nucleosynthesis (BBN), the Cosmic Microwave Background (CMB) and Baryon Acoustic Oscillations (BAO), the Hubble parameter at high z is determined to be [2]

$$H_0 = (67.4 \pm 0.5) \,\mathrm{km/s/Mpc},$$
 (1.1)

while the low z value arising from the analysis of Cepheids and SNIa gives [1]

$$H_0 = (73.04 \pm 1.04) \,\mathrm{km/s/Mpc},$$
 (1.2)

which leads to a 5σ difference between the Planck result and the result arising from local observation. Since the Planck analysis is based on the Λ CDM model, the discrepancy between the high z and the low z results represents an indication of physics beyond the standard Λ CDM model. There is a large number of theory models which attempt to explain this difference (for a review see ref. [3] and references therein, e.g., ref. [4]). One of the simplest avenues is the possibility of having extra relativistic degrees of freedom present during recombination, which would cause an increase in H_0 and bring it closer to its measured local value. Extensions of the SM with new particles in thermal equilibrium with the neutrinos,

such as a majoron [5, 6], or with an extra U(1) symmetry and Z' bosons decaying to neutrinos or otherwise [7, 8] can explain the tension. We note here that models that can successfully explain the Hubble tension are those where the extra degrees of freedom would affect only the dynamics in the CMB era, but not impact BBN. This is so because the precise predictions of light element synthesis during BBN can be translated into strong constraints on the effective degrees of freedom such that $N_{\rm eff}^{\rm BBN}=2.88\pm0.27$ at 68% C.L. [9, 10]. This appears to be consistent with the SM prediction of $N_{\rm eff}^{\rm SM}\simeq3.046$ [11]. Since the effective degrees of freedom are tied to the energy density in the universe, which affects the Hubble parameter, any deviation from $N_{\rm eff}$ at BBN would have an impact on the expansion rate of the universe as well as on predictions of light element synthesis during this epoch. Thus any model looking to add extra relativistic degrees freedom at CMB time to help alleviate the Hubble tension should not violate the BBN constraints on N_{eff} .

Further, $N_{\rm eff}$ is also constrained, but to a lesser extent, during the period the CMB was generated. This is so because extra relativistic degrees of freedom affect the CMB power spectrum, which has been measured using Planck polarization data and BAO, so that [2]

$$N_{\text{eff}} = 2.99^{+0.34}_{-0.33}$$
 (95% C.L., TT,TE,EE+lowE+lensing+BAO). (1.3)

Two earlier local measurements of H_0 [12, 13] (dubbed R18 and R19) have shown an increasing discrepancy with high redshift values of H_0 at 3.7σ and 4.4σ deviation, respectively. The preferred $N_{\rm eff}$ value, when combining the local measurements of H_0 with Planck and BAO data, becomes [2]

$$N_{\text{eff}} = 3.27 \pm 0.15$$
 (68% C.L., TT,TE,EE+lowE+lensing+BAO+R18). (1.4)

Extra relativistic degrees of freedom, $\Delta N_{\rm eff}$, increase the sound horizon r_* during recombination. Since the acoustic scale $\theta_* = r_*/D_M$ is precisely measured, then $D_M \propto 1/H_0$ must decrease, or H_0 must increase to keep inline with experimental measurements. Based on the difference between the early and local measurements of H_0 , it was suggested that

$$0.2 \lesssim \Delta N_{\text{eff}} \lesssim 0.5 \text{ (CMB+BAO+R18), [2]}$$
 (1.5)

and

$$0.2 \lesssim \Delta N_{\text{eff}} \lesssim 0.4$$
 (CMB+BAO+Pantheon [14]+R19+BBN), [15–17] (1.6)

could relax the Hubble tension between high redshift values of H_0 and the local R18 and R19 measurements.² In light of the most recent measurement of H_0 by the SH0ES collaboration [1] one can expect a revised range in order to accommodate higher values of $\Delta N_{\rm eff}$.

In this work we present a cosmologically consistent model based on the Stueckelberg extension of the SM with a hidden sector to help alleviate the Hubble tension between the high and the low z measurements. By a cosmologically consistent model we mean that we take into account the fact that the hidden sector and the visible sector in general live in different heat baths at different temperatures and the Boltzmann equations that evolve the number density of the particle species in the visible and in the hidden sectors must use a two-temperature evolution which, however, are correlated because of the couplings between the two sectors. Thus the hidden sector possesses a $U(1)_X$ gauge symmetry and the couplings between the hidden $U(1)_X$ and the hypercharge $U(1)_Y$ can occur via kinetic mixing and Stueckelberg mass

 $^{^1}D_M = \int_0^{z_*} dz/H(z)$, where z_* is the redshift at the time of last scattering. ²For an estimate of the Hubble parameter in different cosmologies using the Pantheon data, see refs. [18, 19].

mixing. We assume that, aside from the $U(1)_X$ gauge field (which gives the dark photon γ'), the hidden sector contains a Dirac fermion D, a scalar field S and a pseudo-scalar field ϕ . The coupling between the visible sector and the hidden sector is assumed feeble while that between the dark fermion and the dark photon could be of normal size, i.e., of size $\mathcal{O}(1)$. Assuming that there was no initial particle density of the hidden sector particles, the feeble interactions due to small kinetic mixing between the hidden sector $U(1)_X$ and the visible sector $U(1)_Y$ gauge groups allow for a gradual buildup of particle density in the hidden sector. Dirac fermions D (which act as dark matter) and dark photons γ' can be generated from the SM via $2 \to 2$ and $2 \to 1$ processes. The U(1)_X gauge coupling q_X is assumed strong enough to allow D and γ' to enter into chemical equilibrium in the dark sector. It is to be noted that just like the SM thermal bath of massless photons, the dark sector can generate its own thermal bath which we assume here to consist of massless pseudoscalar particle ϕ . Along with ϕ , a light long-lived scalar particle S can be produced. Both ϕ and S have no direct couplings with the SM and are produced purely through dark sector interactions, which we assume to be at a different temperature than for the SM. The resolution of the Hubble tension comes from the decay $S \to \phi \phi$ prior to recombination, which adds to the relativistic degrees of freedom at this epoch and drive the Hubble parameter to larger values. Particle physics models that attempt to explain the Hubble tension either assume the visible and the hidden sectors are initially in thermal contact and decouple later or they start as outof-equilibrium systems and eventually a hidden sector particle thermalizes with the neutrino sector before decaying close to recombination. Our analysis does not involve the neutrinos and the resolution of the Hubble tension comes entirely from the dark sector. Further, the model discussed here can explain the Hubble tension while preserving BBN predictions due to the fact that the particles S and ϕ do not trace their equilibrium distributions in the dark sector owing to the small coupling between them and D and γ' . The model parameters are constrained by the DM relic density, limits on the dark photon mass, and by the chemical and kinetic decoupling of the species and $\Delta N_{\rm eff}$ at BBN.

The paper is organized as follows. In section 2 we give an overview of the model used in the analysis. In section 3 we discuss the set of coupled Boltzmann equations used to evolve the particle yields and the temperatures of the visible and hidden sectors. A discussion of kinetic decoupling of hidden sector particles is given in section 4. In section 5 we give a numerical analysis of the particle yields and the temperature evolution of the sectors taking into accounts the relevant experimental constraints. A discussion on the different contributions to $\Delta N_{\rm eff}$ is given in section 6 followed by an analysis of energy densities and $\Delta N_{\rm eff}$ up to recombination in section 7. Conclusions are given section 8. Further detail of the analysis is given in section 9.

2 The model

We now briefly describe the hidden sector model and its coupling to the visible sector which is used in the analysis of this work. The model is a $U(1)_X$ extension of the SM gauge group which has gauge kinetic mixing [20, 21] between the two abelian gauge groups. The new gauge field obtains its mass through the Stueckelberg mechanism [22, 23] for the gauge fields. Thus the extended model has the Lagrangian

$$\mathcal{L} = \mathcal{L}_{SM} + \Delta \mathcal{L}, \tag{2.1}$$

where \mathcal{L}_{SM} is the Standard Model Lagrangian, and

$$\Delta \mathcal{L} = -\frac{1}{4}C_{\mu\nu}C^{\mu\nu} + i\bar{D}\gamma^{\mu}\partial_{\mu}D - m_{D}\bar{D}D - \frac{1}{2}(\partial_{\mu}\phi\partial^{\mu}\phi) - \frac{1}{2}(\partial_{\mu}S\partial^{\mu}S)$$
$$+ g_{X}Q_{X}\bar{D}\gamma^{\mu}DC_{\mu} + y_{\phi}\bar{D}\gamma_{5}D\phi + y_{S}D\bar{D}S$$
$$-\frac{\delta}{2}C_{\mu\nu}B^{\mu\nu} - \frac{1}{2}(\partial_{\mu}\sigma + M_{1}C_{\mu} + M_{2}B_{\mu})^{2}, \tag{2.2}$$

contains additional terms arising from the hidden sector and its coupling to the visible sector through kinetic energy mixing and Stueckelberg mass mixing. In eq. (2.2), C_{μ} is the gauge field of the U(1)_X and B_{μ} is the gauge field of the U(1)_Y and $C_{\mu\nu} = \partial_{\mu}C_{\nu} - \partial_{\nu}C_{\mu}$ and $B_{\mu\nu} = \partial_{\mu}B_{\nu} - \partial_{\nu}B_{\mu}$. The axionic field σ transforms dually under U(1)_X and U(1)_Y so that the mass term remains gauge invariant and can be discarded in the unitary gauge. The dark fermions, with a charge Q_X under U(1)_X, interact with the gauge field C_{μ} via the gauge interaction with strength g_X , and with the (pseudo-)scalar field (ϕ) S with strength (y_{ϕ}) y_S . We assume a kinetic mixing between the hypercharge field B_{μ} and the U(1)_X gauge field C_{μ} characterized by the mixing parameter δ . The mass growth for the gauge field occurs via the Stueckelberg mechanism and is characterized by the parameters M_1 and M_2 . The scalar sector of the model contains the SM Higgs boson, S and ϕ . Therefore, the scalar potential is given by

$$V = V_{\rm SM} + \frac{1}{2}m_S^2 S^2 + \frac{\kappa_S}{3}S^3 + \frac{\kappa_{\phi S}}{2}\phi^2 S + \frac{\lambda_S}{4}S^4 + \frac{\lambda_{\phi}}{4}\phi^4 + \frac{\lambda_{\phi S}}{2}\phi^2 S^2. \tag{2.3}$$

The mixing between the gauge field B_{μ} and C_{μ} in the Stueckelberg mass mixing term will give the dark fermions a millicharge, which is constrained by several experiments. For simplicity here we set $M_2 = 0$. After electroweak symmetry breaking and in the canonical basis where the kinetic energies of the gauge fields are diagonalized and normalized, we have the following set of couplings among particles of the dark sector and among particles of the dark sector and of the visible sector so that

$$\Delta \mathcal{L}^{\text{int}} = \bar{D}\gamma^{\mu} (g_{\gamma'}^D A_{\mu}^{\gamma'} + g_Z^D Z_{\mu} + g_{\gamma}^D A_{\mu}^{\gamma}) D + \frac{g_2}{2\cos\theta} \bar{\psi}_f \gamma^{\mu} \Big[(v_f' - \gamma_5 a_f') A_{\mu}^{\gamma'} \Big] \psi_f, \tag{2.4}$$

where f runs over all SM fermions. In the limit of small kinetic mixing, $g_{\gamma'}^D \simeq g_X Q_X$ which is a normal strength coupling. The couplings g_Z^D and g_γ^D are given in appendix B. The vector and axial couplings are given by

$$v'_{f} = -\cos\psi[(\tan\psi - s_{\delta}\sin\theta)T_{3f} - 2\sin^{2}\theta(-s_{\delta}\csc\theta + \tan\psi)Q_{f}],$$

$$a'_{f} = -\cos\psi(\tan\psi - s_{\delta}\sin\theta)T_{3f},$$
(2.5)

where $s_{\delta} = \sinh(\delta)$, T_{3f} is the third component of isospin, Q_f is the electric charge for the fermion and the angles θ and ψ are defined in appendix B. We also record here the couplings of the Z_{μ} and A_{μ}^{γ} in the canonically diagonalized basis which are given by [24, 25]

$$\Delta \mathcal{L}'_{SM} = \frac{g_2}{2\cos\theta} \bar{\psi}_f \gamma^\mu \Big[(v_f - \gamma_5 a_f) Z_\mu \Big] \psi_f + e \bar{\psi}_f \gamma^\mu Q_f A_\mu^\gamma \psi_f \,. \tag{2.6}$$

Modifications to the visible sector interactions appear in the vector and axial couplings so that

$$v_f = \cos \psi [(1 + s_\delta \tan \psi \sin \theta) T_{3f} - 2\sin^2 \theta (1 + s_\delta \csc \theta \tan \psi) Q_f],$$

$$a_f = \cos \psi (1 + s_\delta \tan \psi \sin \theta) T_{3f}.$$
(2.7)

Further details can be found in refs. [26–29]. The free parameters of the model described above are subject to a number of theoretical and experimental constraints. The theoretical constraints require that the model produce the desired amount of dark matter, which in turn necessitates a careful analysis of chemical and kinetic decoupling of different particle processes. It also requires that the model maintains the success of the BBN analysis within the SM paradigm, i.e., that the model produces only negligible extra relativistic degrees of freedom at BBN time, but makes a significant contribution $\Delta N_{\rm eff}$ at the time the CMB was produced. These put severe constraints on the dark photon mass, the mass of the dark fermion, and on chemical and kinetic decoupling of species in the dark sector. Additionally, the kinetic mixing and the dark photon mass are severely constrained by current experiments. Despite all the stringent constraints, we show that a considerable parameter space remains viable to construct a cosmologically consistent particle physics model that can help reduce the Hubble tension.

3 Evolution of hidden and visible sector temperatures

Hidden and visible sectors in general reside in heat baths at different temperatures [26, 28, 30–32]. In models of the type we consider, the bath for the hidden sector is at a much lower temperature than the bath for the visible sector. However, because of the coupling between the visible and the hidden sectors, their temperature evolution is correlated. Specifically, the entropy in each sector is not separately conserved, but it is only the total entropy that is conserved. Thus the total entropy is $S = \mathfrak{s}R^3$, where R is the scale factor and $\mathfrak{s} = \mathfrak{s}_v + \mathfrak{s}_h$, where \mathfrak{s}_h is the hidden sector entropy density, \mathfrak{s}_v is the entropy density of the visible sector, and

$$s = \frac{2\pi^2}{45} \left(h_{\text{eff}}^h T_h^3 + h_{\text{eff}}^v T^3 \right). \tag{3.1}$$

Here h_{eff}^v and h_{eff}^h are the visible and the hidden effective entropy degrees of freedom and T (T_h) is the temperature of the visible (hidden) sector. The conservation of the total entropy leads to the evolution equation for the entropy density

$$d\mathfrak{s}/dt + 3H\mathfrak{s} = 0. \tag{3.2}$$

The temperature evolution of the two sectors is also affected by the dependence of the Hubble parameter on the temperatures of the two sectors. Thus the Friedman equation gives

$$H^{2} = \frac{8\pi G_{N}}{3} (\rho_{v}(T) + \rho_{h}(T_{h})), \tag{3.3}$$

where $\rho_v(T)$ and $\rho_h(T_h)$ are the energy densities of the visible and of the hidden sectors and are given in terms of their respective energy density degrees of freedom as

$$\rho_v = \frac{\pi^2}{30} g_{\text{eff}}^v T^4, \quad \rho_h = \frac{\pi^2}{30} g_{\text{eff}}^h T_h^4. \tag{3.4}$$

For the visible sector effective degrees of freedom, g_{eff}^v and h_{eff}^v , the recent tabulated results from lattice QCD [33] are used, while for the hidden sector, g_{eff}^h and h_{eff}^h are given in the form of integrals in appendix A. The time evolution of the energy density in the hidden sector is given by

$$\frac{d\rho_h}{dt} + 3H(\rho_h + p_h) = j_h,\tag{3.5}$$

where p_h is hidden sector pressure density and j_h is the source in the hidden sector. It encodes the heat exchange between the visible and the hidden sectors and is given by eq. (3.7) of appendix \mathbb{C} .

Since the temperatures of the visible and the hidden sectors are correlated, a quantitative analysis of this correlation is essential. For this reason we introduce a function $\eta = T/T_h$. The evolution equation for η depends on the particle number densities, and so we need to identify the interactions that enter in the evolution. There are two such types of interactions. The first one involves the interactions of the dark particles among themselves, i.e., among D, D, γ', ϕ and S. Then we have the feeble interactions between the visible sector and the hidden sector, which involve processes of the type $i\bar{i} \to DD$, and $i\bar{i} \to \gamma'$, where i refers to the Standard Model particles and the interactions are those induced by the kinetic energy mixing. We assume no initial number density for the hidden sector particles and it is only through the feeble interactions of the visible sector with the hidden sector that the hidden sector particles are produced. Here we note that only D, D and γ' are produced by the portal interactions with the visible sector, while ϕ and S are only produced by interactions within the dark sector. The set of all interactions considered appear in the system of coupled Boltzmann equations, eqs. (C.1)-(C.4) (see appendix C). Here we have introduced the dimensionless quantity $Y_a = n_a/s$, the comoving number density or yield of a particle species a, and have written the equations relative to the hidden sector temperature T_h instead of time.

The ratio $\eta \equiv T/T_h$ is itself dependent on T_h , since we have taken T_h as our reference temperature. Its evolution is driven by the energy injection from the SM into the dark sector. The energy exchange is given by the source term j_h . In this case one may derive the equation for η so that

$$\frac{d\eta}{dT_h} = -\frac{\eta}{T_h} + \left[\frac{\zeta \rho_v + \rho_h(\zeta - \zeta_h) + j_h/(4H)}{\zeta_h \rho_h - j_h/(4H)} \right] \frac{d\rho_h/dT_h}{T_h(d\rho_v/dT)},\tag{3.6}$$

where j_h is given by

$$j_h = \sum_i \left[2Y_i^{\rm eq}(T)^2 J(i \; \bar{i} \to D\bar{D})(T) + Y_i^{\rm eq}(T)^2 J(i \; \bar{i} \to \gamma')(T) \right] s^2 - Y_{\gamma'} J(\gamma' \to f\bar{f})(T_h) s. \tag{3.7}$$

The J terms appearing in eq. (3.7) are given in appendix C. In eq. (3.6), ζ and ζ_h are 1 for the radiation dominated era and 3/4 for matter dominated era. More generally they are given by $\zeta = \frac{3}{4}(1 + p_v/\rho_v)$ and $\zeta_h = \frac{3}{4}(1 + p_h/\rho_h)$.

The relic density of D, which is dark matter, is related to Y_D^{∞} , the yield today, and the entropy density today, \mathfrak{s}_0 by

$$\Omega h^2 = \frac{m_D Y_D^{\infty} \mathfrak{s}_0 h^2}{\rho_c},\tag{3.8}$$

where ρ_c is the critical density, and h = 0.674 [2]. The total relic density of dark matter as given by the Planck collaboration [34] is $(\Omega h^2)_{\rm PLANCK} = 0.1198 \pm 0.0012$. Note that since we are modifying the early cosmology of $\Lambda {\rm CDM}$ by adding extra radiation, the DM relic density is bound to change. This is taken into consideration in the numerical analysis as we explain later.

4 Departure from kinetic equilibrium

As the temperature of the universe drops, annihilation processes (i.e., number-changing processes) become progressively inefficient. Once their rate falls below the Hubble expansion rate, the involved particle species undergo chemical decoupling. The onset of chemical decoupling between D and γ' in the dark sector initiates a dark freeze-out where the dark matter yield or comoving number density remains fixed with falling temperature. Despite this decoupling, particle species can remain in local thermal equilibrium through scattering processes with the thermal bath. Focusing on D, its temperature T_D still follows that of the hidden sector's thermal bath $T_h = T_\phi$ as it scatters off relativistic species, namely S and ϕ , via the processes $DS \to DS$ and $D\phi \to D\phi$. The same holds for S: after its chemical decoupling, local thermal equilibrium can be maintained via $S\phi \to S\phi$. Even those processes will eventually lose their competition against the Hubble rate and decouple. Note that kinetic decoupling can occur before chemical decoupling in which case one needs to solve the full Boltzmann equations for the phase space distributions [35, 36]. This has an effect on the relic density and is often numerically challenging. Here we restrict ourselves to the case where kinetic decoupling happens much after chemical decoupling has occurred which is the assumption made when writing the Boltzmann equations, eqs. (C.1)–(C.4).

To determine the temperature of kinetic decoupling of a dark sector species X with mass m_X , one needs to solve the second moment of the Boltzmann equation. An analytical solution is quite complicated but can be simplified by assuming that the scattering particle is non-relativistic which means that $T_X \ll m_X$ and that the typical momentum transfer in the scattering processes is small compared to m_X . Keeping only leading order terms in p^2/m_X^2 , we write the Boltzmann equation as [37, 38]

$$(\partial_t + 5H)T_X = 2m_X \gamma(T_\phi)(T_\phi - T_X), \tag{4.1}$$

where $\gamma(T_{\phi})$ is the momentum transfer rate evaluated at the bath temperature T_{ϕ} , T_X is the temperature of particle X (used to describe departure from kinetic equilibrium) with number density n_X , and is defined by

$$T_X = \frac{1}{3m_X n_X} \int \frac{d^3 p}{(2\pi)^3} p^2 f(p), \tag{4.2}$$

where f(p) is the one particle phase space distribution and the Hubble parameter is given by

$$H^{2}(T_{\phi}) = \frac{4\pi^{3}}{45M_{\text{DI}}^{2}} (g_{\text{eff}}^{v} \eta^{4} + g_{\text{eff}}^{h}) T_{\phi}^{4}. \tag{4.3}$$

The momentum transfer rate in eq. (4.1) is given in terms of an average of the matrix element squared over the Mandelstam variable t [39]

$$\gamma(T_{\phi}) = \frac{g_{\phi}}{384\pi^{3} m_{X}^{4} T_{\phi}} \int dE \, f^{\pm}(E) (1 \mp f(E)) \int_{-4k^{2}}^{0} (-t) |\mathcal{M}|^{2} \, dt, \tag{4.4}$$

where E is the energy of the bath particle ϕ with $g_{\phi} = 1$. The upper sign in $f^{\pm}(E)(1 \mp f(E))$ correspond to fermions and the lower sign to bosons. The temperature of kinetic decoupling $T_{\rm kd}$ is calculated as

$$\gamma(T_{\phi}) = H(T_{\phi})\Big|_{T_{\phi} = T_{kd}},\tag{4.5}$$

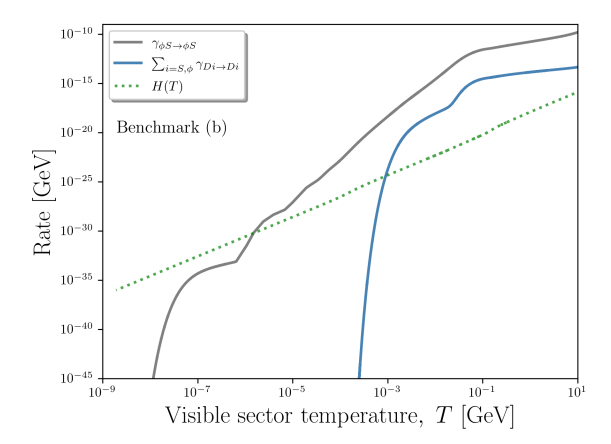


Figure 1. Momentum transfer rates for $D\phi \to D\phi$, $DS \to DS$ (blue curve) and $\phi S \to \phi S$ (gray curve) along with the Hubble rate (dashed line) as a function of the visible sector temperature. For this set of parameters corresponding to benchmark (b) in table 1, $T_{\rm kd}^D > T_{\rm kd}^S$.

assuming instantaneous decoupling. Prior to decoupling, T_X traces T_ϕ as both temperatures drop as 1/R. However, after decoupling, the temperature of X (D and S in our model) decreases as $1/R^2$, while T_ϕ continues as 1/R assuming that there are no further interactions or decays. This situation will change in the next section when we discuss out-of-equilibrium decay of S, which adds to the energy density of ϕ . An illustration of how eq. (4.5) works is given in figure 1, where we show the rate of the processes $D\phi \to D\phi$, $DS \to DS$ (blue curve) and $\phi S \to \phi S$ (gray curve) along with the Hubble parameter (dashed line) plotted against the visible sector temperature. Kinetic decoupling occurs when the rate falls below H(T) which for D occurs at a higher temperature than that for S for this particular choice of parameters (benchmark (b) of table 1 below).

Note that our model predicts late kinetic decoupling, while there exists a lower limit on $T_{\rm kd}$ from Lyman- α forest measurements [40] implying that $T_{\rm kd} > 100\,{\rm eV}$. This will set constraints on the couplings in the dark sector.

5 Numerical analysis: yield and temperature evolution prior to decoupling

In this section we discuss the results pertaining to temperature and number density evolution before the full decoupling of the dark sector species. Here we numerically solve the coupled Boltzmann equations, eqs. (C.1)–(C.4), together with the temperature evolution of the two sectors, eq. (3.6), in order to track the growth of the particle yields as a function of the temperature T_h . The system of equations form a set of stiff differential equations which are solved in two steps: (1) integrating from a high temperature assuming $T_h/T \ll 1$ until chemical decoupling sets in the dark sector at $T_{\rm cd}$ and (2) integrating dY_S/dT_h and dY_ϕ/dT_h from $T_{\rm cd}$ down to 1 eV assuming Y_D = constant and $Y_{\gamma'}=0$. In every calculation we verified that $Y_{\gamma'}$ is small enough to be discarded (since γ' decays away before BBN) and that D has already undergone a dark freeze-out. Splitting the temperature range this way helps the ordinary differential equation solver tackle the stiffness of the system at hand.

Benchmark (c)

 $\Omega h^2 = 0.12$

Model	m_D	$m_{\gamma'}$	m_S	δ	y_S	$\kappa_{\phi S} \; [\text{GeV}]$	$\lambda_{\phi S}$	$\Delta N_{ m eff}^{ m CMB}$
(a)	0.1	0.9	10^{-2}	4.6×10^{-11}	3.0×10^{-3}	1.9×10^{-18}	1.0×10^{-7}	0.43
(b)	0.3	0.2	10^{-2}	1.6×10^{-9}	1.0×10^{-3}	6.0×10^{-18}	5.0×10^{-6}	0.55
(c)	0.6	0.5	10^{-3}	6.0×10^{-10}	3.0×10^{-3}	3.3×10^{-19}	5.0×10^{-7}	0.36
(d)	1.0	0.3	10^{-2}	1.7×10^{-9}	5.0×10^{-3}	8.5×10^{-19}	1.0×10^{-8}	0.54

Table 1. Selection of benchmarks used in this analysis. We have set $\epsilon = M_2/M_1 = 0$, $\kappa_S = 10^{-18}$ GeV, $y_{\phi} = 0$ and $g_X = 0.0125$. All masses are in GeV.

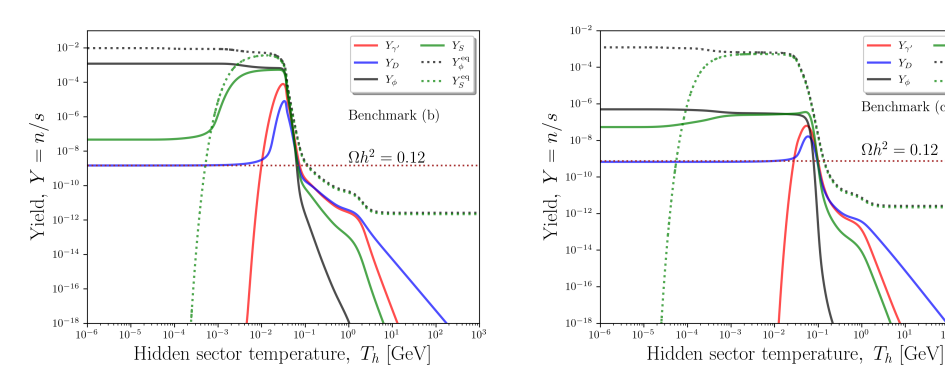
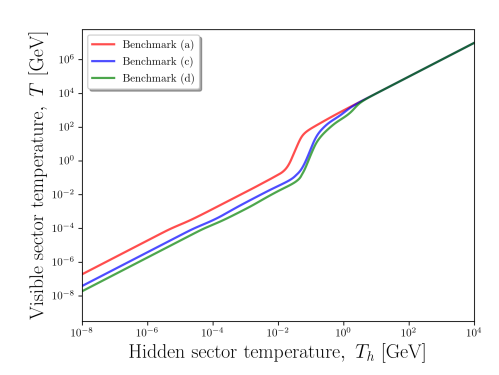


Figure 2. Evolution of the hidden sector particle yields (solid lines) as a function of the hidden sector temperature for benchmark (b) (left panel) and benchmark (c) (right panel) of table 1. The dashed curves correspond to the equilibrium distribution of the particles S and ϕ . Here $(\Omega h^2)_D \simeq 0.12$.

We select a set of representative benchmarks which satisfy all the experimental constraints on the dark matter relic density and the dark photon mass and which can help alleviate the Hubble tension. They are given in table 1. Note that a more general investigation of the available parameter space will be given later in this section and in the next sections as well. The DM relic density for benchmarks (b)-(d) is ~ 0.12 while that for (a) is 0.07 which can be explained by the smallness of the kinetic mixing δ . We note here that κ_s and $\kappa_{\phi s}$ have dimension of mass and one expects these to be Planck suppressed so that the first such term is of size $\lambda m_{\rm EW}^2/m_{\rm Pl}$. For $m_{\rm EW}\sim 10^2\,{\rm GeV},\,m_{\rm Pl}\sim 10^{19}\,{\rm GeV},\,{\rm and}\,\,\lambda\sim 10^{-3}$ one gets $\kappa \sim \kappa_{\phi s} \sim 10^{-18} \, \text{GeV}$.

We show in figure 2 the evolution of the particle yields as a function of the hidden sector temperature for benchmarks (b) (left panel) and (c) (right panel). The solid lines correspond to the particle yields as obtained from solving the Boltzmann equations, while the dotted lines correspond to the equilibrium yields of ϕ and S. One can see from the left panel that the particle yields increase gradually with D and γ' taking the lead as they are produced by SM processes while the yields for S and ϕ are smaller since they are produced only via their interactions with D and with each other (see eqs. (C.1) and (C.2)). The yields undergo a sudden surge at $T_h \sim 0.1 \,\text{GeV}$ which happens near the QCD crossover $(T = \eta T_h < 1 \,\text{GeV})$ where the freeze-out of the SM degrees of freedom causes an entropy dump leading to a sudden drop in the visible sector temperature relative to the hidden sector. One can see in the left panel of figure 3 that the visible temperature drops sharply at $T \sim 1 \text{ GeV}$ while the



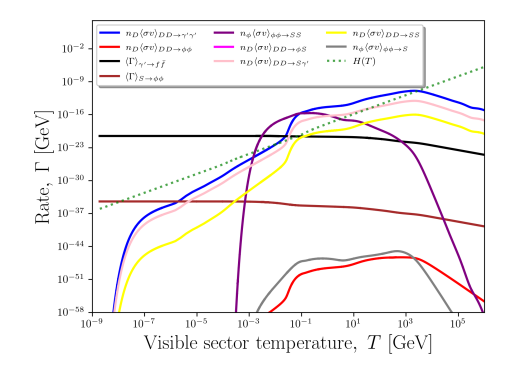


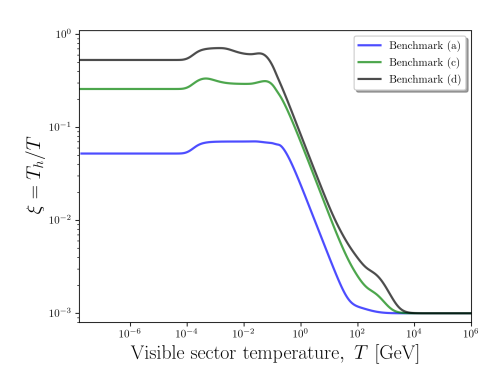
Figure 3. Left panel: variation of the visible sector temperature as a function of the hidden sector temperature for benchmarks (a), (c) and (d) of table 1. Right panel: rates for the different processes that enter into the Boltzmann equation (solid curves) as compared to the Hubble rate (dashed line) plotted as a function of the visible sector temperature.

hidden sector temperature drops at a slower rate. This can be seen using the conservation of entropy

$$S = \frac{2\pi^2}{45} [h_{\text{eff}}^v \eta^3 + h_{\text{eff}}^h] T_h^3 R^3 = \frac{2\pi^2}{45} [h_{\text{eff}}^v + h_{\text{eff}}^h \xi^3] T^3 R^3 = \text{const.}$$
 (5.1)

Not only does h_{eff}^v undergo a sudden drop, but so does η (see right panel of figure 4). As a result, one can immediately see from the first equality of eq. (5.1) that T_h drops at a slower rate. On the contrary, the second equality of eq. (5.1) shows that a drop in h_{eff}^v is partially compensated by an increase in the second term proportional to ξ , where we define $\xi \equiv 1/\eta$ (see left panel of figure 4). As a result, the drop in the visible sector temperature is not slowed down. Following this increase, the yield of γ' starts decreasing (red curve) as the decay rate overtakes the Hubble parameter (see black curve in the right panel of figure 3). At the same time dark matter annihilation in the dark sector becomes very efficient, leading to a drop in the dark matter yield (blue curve) before freeze-out sets in as the rate of the process $D\bar{D} \to \gamma' \gamma'$ drops below the Hubble rate. At this point, D and γ' are chemically decoupled after they have been in chemical equilibrium for some time, as seen in the right panel of figure 3, leading to dark matter freeze out and the yield leveling off. Note that this happens at $T_h \sim 10^{-2}\,\text{GeV}$ which is in the neighborhood of $m_D/20$, the standard freeze-out temperature.

We also notice from the right panel of figure 3 that ϕ and S enter into chemical equilibrium (purple curve) as well as D, γ' and S (pink curve). Thus there is a period in the thermal history of the dark sector where all species are in thermal equilibrium. Chemical decoupling between ϕ and S happens after chemical decoupling of D and γ' and so the freeze-out of S happens at a lower temperature. From the left panel of figure 2, the yield of S can be seen leveling off at $T_h \sim 5 \times 10^{-4}$ GeV. The drop in the yield of S is followed by a rise in ϕ before the yield of the latter continues at a fixed value. Notice that neither S nor ϕ follow their equilibrium distribution (plotted as dotted curves) which is an essential criterion in our analysis to avoid the BBN constraint on $\Delta N_{\rm eff}$ as we discuss later. We note also that S does not contribute to the relic density, since it will eventually decay near recombination as the rate of $S \to \phi \phi$ overtakes the Hubble rate (see right panel of figure 3).



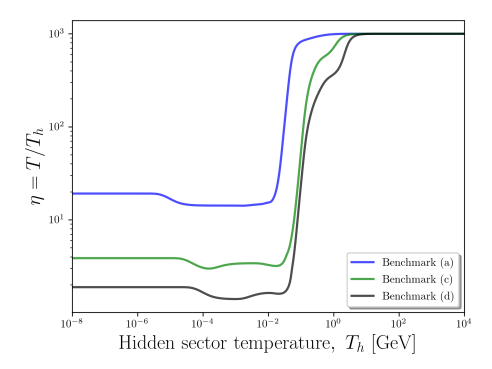


Figure 4. Left panel: evolution of the hidden sector temperature represented by $\xi \equiv 1/\eta$ as a function of the visible sector temperature for benchmarks (a), (c) and (d) of table 1. Right panel: the ratio η as a function of the hidden sector temperature for the same benchmarks.

The energy injection from the SM into the cold dark sector gradually causes its temperature to increase. This is depicted in the left panel of figure 4 for benchmarks (a), (c) and (d) of table 1. For those benchmarks, the two sectors do not thermalize and ξ reaches at most a value ~ 0.55 (for benchmark (d)) after BBN. The degree at which the two sectors reach thermal equilibrium depends on the size of the kinetic mixing δ which is why benchmark (a) has the smallest ξ value since it has the smallest δ . A larger value of δ can produce a thermal distribution of ϕ , and for ξ large enough contributions to $\Delta N_{\rm eff}$ at BBN can be sizable which implies that δ is constrained in order to maintain the successful BBN predictions of the SM.

We now discuss the available parameter space of the model taking into account the dark matter relic density constraint and limits on the dark photon mass. For a fixed value of m_D and q_X , we scan the parameter space in the kinetic mixing-dark photon mass plane. We only keep points that satisfy the dark matter relic density, $(\Omega h^2)_D \sim 0.1$ –0.125,³ and ones where kinetic decoupling of D happens after its chemical decoupling. We also remove points with very late kinetic decoupling of S and those with $\Delta N_{\rm eff}^{\rm BBN} > 0.2$. Further, there is an array of experimental limits on the dark photon mass which mixes kinetically with the SM sector. These include CHARM [41, 42], E141 [43] and ν -CAL [42, 44–47], E137 [48, 49], electron and muon g - 2 [50], BaBar [51], NA48 [52], NA64 [53, 54], E141 [43] and LHCb [55, 56]. The limits are obtained from darkcast [57]. Additionally, more stringent constraints arise from Supernova SN1987A [58] and BBN. The experimental limits as well as the region resulting from a scan of our model are presented in figure 5. In the top left panel of figure 5 we exhibit the case for $m_D = 0.1 \,\text{GeV}$, and in the top right panel the case for $m_D = 0.3 \,\text{GeV}$. In bottom left panel we exhibit the case for $m_D = 0.6 \,\mathrm{GeV}$, and in the bottom right panel the case for $m_D = 1.0 \,\mathrm{GeV}$ where for all cases we have $g_X = 0.0125$. The analysis of the panels shows that a part of the parameter space in the range $m_{\gamma'} = 0.1 \,\text{GeV}$ to $1.0 \,\text{GeV}$ is available. Further, in the top panels of figure 5, one finds two allowed regions consistent with all constraints for $\delta \sim \mathcal{O}(10^{-7})$. These regions are in the vicinity of $m_{\gamma'} = 2m_D$ which activates the channel $DD \to \gamma'$ causing a drop in the dark matter relic density. To compensate this, an increase in δ is required.

³The presence of extra radiation causes the DM relic density to increase so that matter-radiation equality is maintained at a fixed redshift. The parameters of our model offer a flexibility when it comes to the dark matter relic density

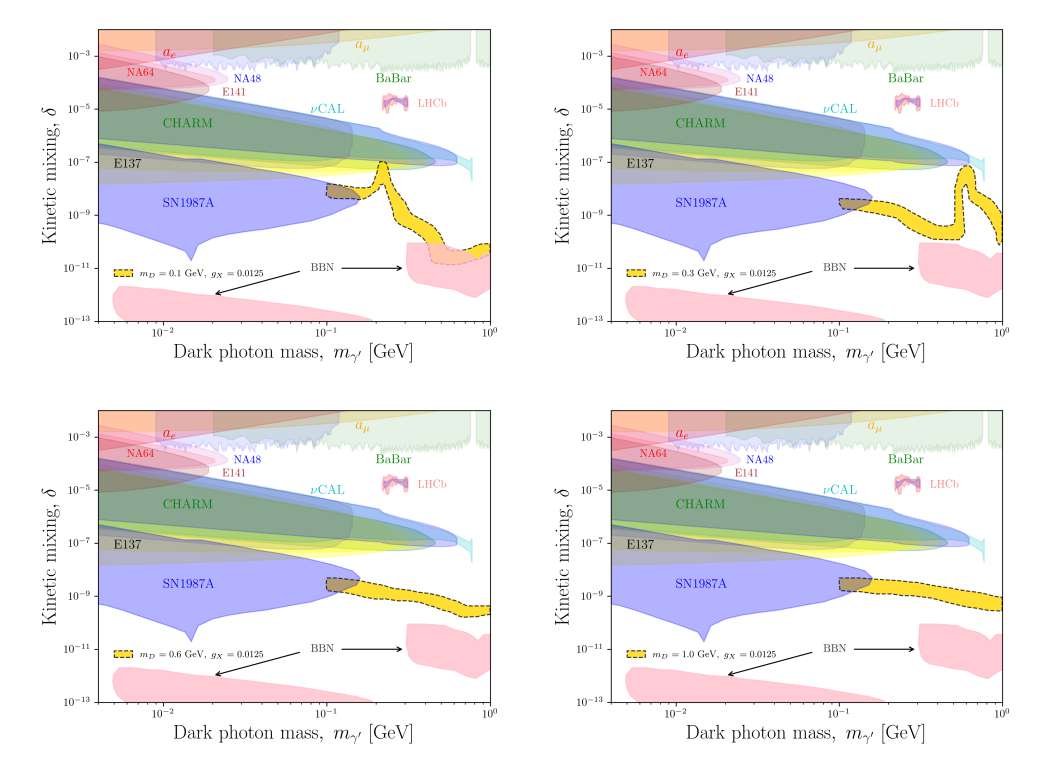


Figure 5. Exhibition of the 2σ regions in the space of the kinetic mixing parameter δ and the dark photon mass $m_{\gamma'}$ for four dark fermion masses: $m_D=0.1\,\mathrm{GeV}$ (top left panel), $m_D=0.3\,\mathrm{GeV}$ (top right panel), $m_D=0.6\,\mathrm{GeV}$ (bottom left panel), and $m_D=1.0\,\mathrm{GeV}$ (bottom right panel). Other parameters are as shown in table 1 for benchmark (a). The regions excluded by several experiments as discussed in text are also exhibited. The analysis shows that there exists a significant region of the parameter space consistent with the experimental constraints which may help alleviate the Hubble tension.

6 Contributions to $\Delta N_{ m eff}$

After neutrino decoupling from photons, the visible sector has two separate thermal baths: the neutrinos with temperature T_{ν} and the photons with temperature T_{γ} , where $T_{\gamma} = (11/4)^{1/3}T_{\nu}$ based on entropy conservation. Note that in principle, the three neutrino species have different temperatures, however, neutrino oscillations tend to thermalize the three flavors and one can describe them by a single temperature. The effective number of relativistic degrees of freedom in the SM is thus given by

$$N_{\text{eff}}^{\text{SM}} = \frac{8}{7} \left(\frac{11}{4}\right)^{4/3} \left(\frac{\rho - \rho_{\gamma}}{\rho_{\gamma}}\right) = 3 \left(\frac{11}{4}\right)^{4/3} \left(\frac{T_{\nu}}{T_{\gamma}}\right)^{4}. \tag{6.1}$$

Precision calculations of N_{eff} give a value slightly different than three, namely $N_{\text{eff}}^{\text{SM}} = 3.046$ [11, 59] after taking into account non-instantaneous decoupling of neutrinos, finite temperature corrections, neutrino oscillations and effects of e^+e^- annihilation to neutrinos.

Deviations from the SM value of $N_{\rm eff}$ can be realized in beyond the SM physics with particles contributing to the energy density of the universe. At BBN time, an increase in $N_{\rm eff}$ (and consequently in the energy density) would increase the expansion rate of the universe leading to observable effects on the light elements' abundances which are successfully predicted by BBN (in particular the Helium mass fraction). Thus, extra relativistic degrees of freedom in a particle physics model must not spoil BBN predictions. Deviations from $N_{\rm eff}^{\rm SM}$ are written as

$$\Delta N_{\text{eff}} \equiv N_{\text{eff}} - N_{\text{eff}}^{\text{SM}} = \frac{8}{7} \left(\frac{11}{4}\right)^{4/3} \frac{\rho_{\text{DS}}(T_h)}{\rho_{\gamma}(T_{\gamma})},$$
 (6.2)

where $\rho_{DS} = \rho_D + \rho_S + \rho_{\phi}$. Here ρ_D and ρ_S are mass densities and are given by $\rho_i = m_i n_i$ (i = D, S). The energy densities of the massless particles are

$$\rho_{\phi}(T_h) = 3n_{\phi}T_h,\tag{6.3}$$

$$\rho_{\gamma}(T_{\gamma}) = \frac{\pi^2}{30} g_{\gamma} T_{\gamma}^4 \,, \tag{6.4}$$

where $g_{\gamma}=2$. For the benchmarks of table 1, $\Delta N_{\rm eff}^{\rm BBN}$ ranges from $\mathcal{O}(10^{-4})$ to $\mathcal{O}(10^{-2})$ which is far too small and thus consistent with $N_{\rm eff}^{\rm SM}$. We emphasize here that the reason for this is having a particle number density in the dark sector that never traces its equilibrium distribution owing to the small coupling between the two sectors. Since at BBN the only particles that are still relativistic are ϕ and S, one can argue that increasing the couplings between D and (ϕ, S) could increase the number densities of the latter causing a conflict with BBN. This, however, reduces the relic density of D. To bring it back up to its experimental value, an increase in δ is required, which is constrained by several experiments as shown in figure 5.

Near recombination, all particles have decoupled from the dark sector bath and ϕ is the only relativistic degree of freedom in the dark sector. Thus, the contribution to $N_{\rm eff}$ following the decay $S \to \phi \phi$ is given by

$$\Delta N_{\text{eff}} = \frac{8}{7} \left(\frac{11}{4}\right)^{4/3} \frac{\rho_{\phi}(T_{\phi})}{\rho_{\gamma}(T_{\gamma})}.$$
 (6.5)

We note here that an important property of ϕ are sufficiently large self-interactions. This is achieved via a four-point contact interaction $\phi\phi\to\phi\phi\propto\lambda_\phi^2$ and via the exchange of S (in both s and t channels), where the latter is proportional to $\kappa_{\phi S}^2$, see eq. (2.3). Self-interactions prevent ϕ from free-streaming which can cause observable effects on the CMB power spectrum [60, 61]. An example in the SM are neutrinos which free-stream after their decoupling from photons. Such a free-streaming leads to a phase shift in the CMB and BAO peaks [60, 62], and the measurements from Planck are sensitive to any deviation in the evolution of perturbations [62–64]. We can estimate the size of the coupling required to achieve efficient self-interactions of ϕ making it an ideal fluid. We will ignore the diagrams that are proportional to $\kappa_{\phi S}^2$ since they are very small (see table 1). The smallness of this coupling ensures that S is long-lived and decays just prior to recombination. Thus, the only diagram remaining is the four-point contact interaction. The interaction rate is given by

$$n_{\phi}(T_{\phi})\langle \sigma v \rangle_{\phi\phi \to \phi\phi} = \frac{9x\lambda_{\phi}^{2}}{64\pi^{2}}T_{\phi}, \tag{6.6}$$

where $x = n_{\phi}/n_{\phi}^{\text{eq}}$. Comparing it to the Hubble rate, we can derive a lower bound on λ_{ϕ} such that

$$\lambda_{\phi}^2 \ge \frac{64\pi^2}{9x} \left(\frac{8\pi^3}{90M_{\rm Pl}^2} g_{\rm eff}\right)^{1/2} \xi^2 T_{\gamma},$$
(6.7)

where $g_{\text{eff}} = g_{\text{eff}}^v + g_{\text{eff}}^h \xi^4$. For $T_{\gamma} \sim 1 \text{ eV}$, $\xi \sim 0.5$ and $x \sim 10^{-2}$, we obtain $\lambda_{\phi} \gtrsim 10^{-12}$. Thus even for such small values of the self-coupling one can achieve efficient self-interactions to prevent the free-streaming of ϕ .

7 Reheating of the dark sector bath prior to recombination

Contributions to ΔN_{eff} at CMB have been considered before in the literature, but only in two contexts: (1) the visible and hidden sectors were initially in thermal contact and decouple later at a temperature T_d causing the temperature of the hidden sector to vary as [65]

$$\frac{T_{\phi}}{T_{\gamma}} = \left[\frac{h_{\text{eff}}^{v}(T_{\gamma})}{h_{\text{eff}}^{h}(T_{d})} \right]^{1/3},\tag{7.1}$$

and (2) the sectors were not in thermal equilibrium but eventually become thermalized [66–68] where a hidden sector particle decays to neutrinos after it becomes non-relativistic [6, 8, 69]. In the model discussed here, the particles in the dark sector are produced exclusively by SM processes. Furthermore, the massive particle S and the relativistic species ϕ in the dark sector are produced in the right amount so as to satisfy BBN constraints while contributing effectively to $\Delta N_{\rm eff}^{\rm CMB}$ which can be obtained entirely due to contributions from the dark sector and without participation of the neutrino sector.

After decoupling of the dark sector species from the visible sector, the main coupled set of Boltzmann equations that we need to solve are

$$\frac{d\rho_S}{dt} + 3H\rho_S = -\Gamma_S \,\rho_S,\tag{7.2}$$

$$\frac{d\rho_{\phi}}{dt} + 4H\rho_{\phi} = \Gamma_S \,\rho_S,\tag{7.3}$$

$$\frac{d\rho_D}{dt} + 3H\rho_D = 0, (7.4)$$

$$\frac{d\rho_{\gamma}}{dt} + 4H\rho_{\gamma} = 0, (7.5)$$

where the Hubble parameter is given by

$$H(T) = \sqrt{\frac{8\pi}{3m_{\rm Pl}^2} (\rho_S + \rho_\phi + \rho_\gamma + \rho_D + 3\rho_\nu)}.$$
 (7.6)

Here, $m_{\rm Pl} = 1.22 \times 10^{19} \, {\rm GeV}$ is the Planck mass and the decay width of $S \to \phi \phi$ is given by

$$\Gamma_S = \frac{\kappa_{\phi S}^2}{32\pi m_S}. (7.7)$$

Adding the Boltzmann equation for neutrinos (and for electrons) does not have any significant impact on the analysis. We integrate the equations from the temperature at which the last

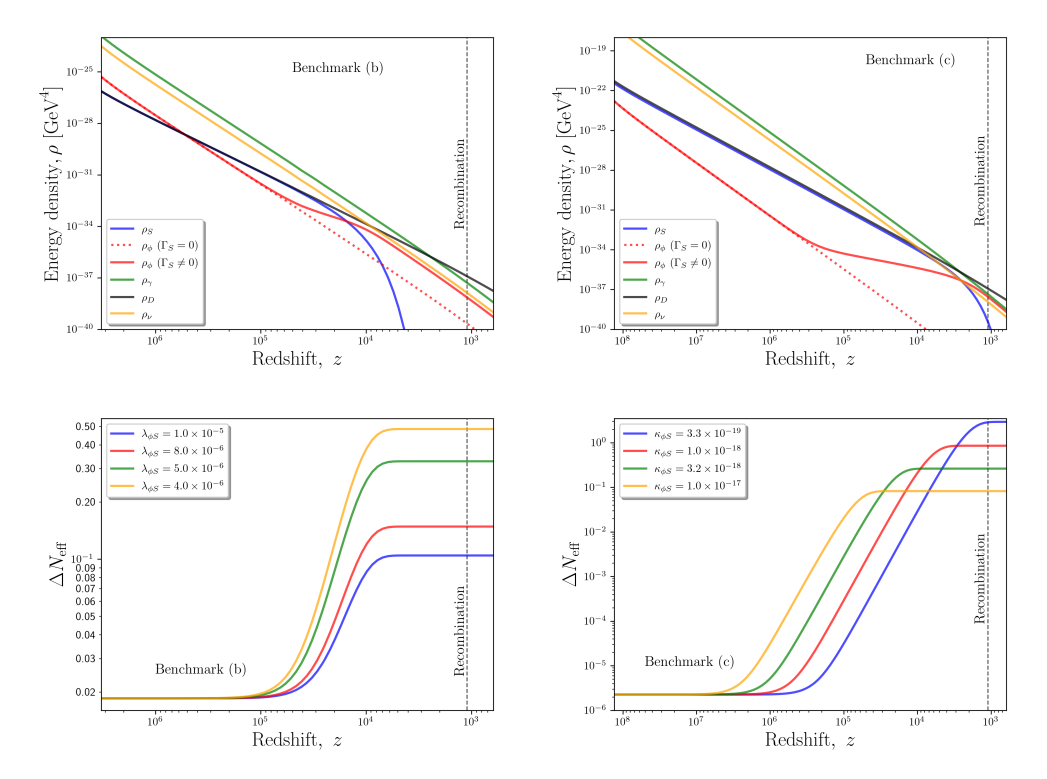
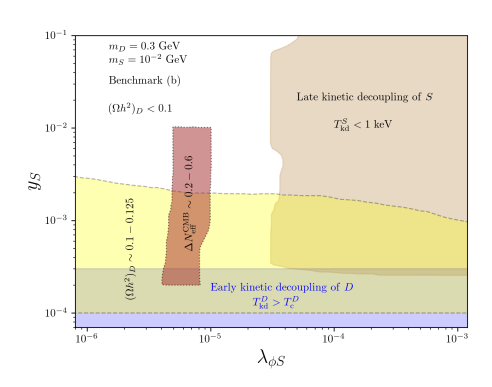


Figure 6. Top panels: evolution of the energy densities of S, ϕ , D, the neutrino and the photon with time for benchmark (b) (left) and benchmark (c) (right), where the dashed line shows ρ_{ϕ} in case S does not decay. Bottom panels: change in $\Delta N_{\rm eff}$ from decoupling to recombination for four values of the coupling $\lambda_{\phi S}$ (left) and for four values of the coupling $\kappa_{\phi S}$ (right). The other parameters are the same as for benchmarks (b) and (c) in table 1.

dark sector particle decouples till the time of recombination, $T_{\gamma} \sim 1\,\mathrm{eV}$. The results for the evolution of the energy densities and ΔN_{eff} with time are shown in figure 6.

In the top panels of figure 6, we exhibit the change in the energy densities as a function of time. One can see that the energy density of ϕ starts to increase as S begins to decay. Eventually ρ_S drops to zero and ρ_ϕ becomes closer to ρ_γ which causes an increase in $\Delta N_{\rm eff}$ according to eq. (6.5). In the bottom panels, we show the variation in $\Delta N_{\rm eff}$ for four choices of the coupling $\lambda_{\phi S}$ (left) and $\kappa_{\phi S}$ (right). Here we see that $\Delta N_{\rm eff}^{\rm CMB}$ can be achieved in the required range of 0.2–0.5 for the chosen parameter set. A smaller $\lambda_{\phi S}$ means the reaction $SS \to \phi \phi$ becomes less efficient leading to more S particles available to decay to ϕ just before recombination which explains the increase in $\Delta N_{\rm eff}^{\rm CMB}$ for smaller $\lambda_{\phi S}$. Furthermore, a smaller $\kappa_{\phi S}$ leads to the same result, i.e., $\Delta N_{\rm eff}^{\rm CMB}$ increases as the decay of S happens closer to recombination.

We present in figure 7 an exclusion limit in the two parameters y_S and $\lambda_{\phi S}$ for benchmark (b) in the left panel and benchmark (c) in the right panel. Similar limits can be realized for the other benchmarks. Here one finds that the parameter space for each $(m_D, m_{\gamma'})$ is constrained by the DM relic density and the requirement on early and late kinetic decoupling



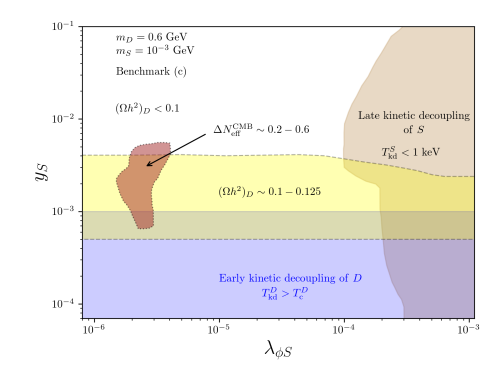


Figure 7. Exclusion limits in the y_S - $\lambda_{\phi S}$ plane for benchmark (b) (left panel) and benchmark (c) (right panel). The overlap between the brown and the yellow regions correspond to a parameter space consistent with all experiments.

of dark sector particles. The region consistent with the DM relic density is shown in yellow and the one which gives $\Delta N_{\rm eff}^{\rm CMB}$ in the right range which may help alleviate the Hubble tension is shown in brown. Points in the overlap region are cosmologically consistent model points able to reduce the Hubble tension while in accordance with BBN constraints on $\Delta N_{\rm eff}$.

Having extra relativistic degrees of freedom from a dark sector (i.e., a dark radiation) will have observable effects on the CMB power spectrum. The cosmological background is blind to the nature of the relativistic species when it comes to its effect on H_0 . Both free-streaming and non-free-streaming dark radiation cause an increase in the expansion rate of the universe prior to matter-radiation equality. This additional radiation pushes more high- ℓ modes to enter the horizon during radiation-domination [70] and since radiation-matter equality is required to occur at a fixed z [61], this creates a degeneracy between extra radiation and the matter density. As a result, the DM relic density is expected to grow. Furthermore, changes in the comoving sound horizons at CMB last scattering (r_*) and baryon drag (r_d) are expected. Because of the stringent constraints from CMB on r_*/D_M (which controls the angular scale of the CMB peaks), a change in the angular diameter distance D_M should occur to keep that ratio fixed. Also, extra radiation is degenerate with the free electron fraction which is correlated with the Helium abundance that is successfully predicted by BBN. All of this shows how the different cosmological parameters are tightly related and to know the extent the additional particles S and ϕ and their dynamics have on these parameters and especially on H_0 would require a more extensive analysis to fit the CMB data.

8 Conclusion

The discrepancy between the high redshift (z > 1000) and the low redshift (z < 1) measurements of the Hubble parameter, which now stands at 5σ , is an important clue to the model underlying the expansion of the universe. At early times, the Hubble parameter is extracted based on the Λ CDM model from measurements of the acoustic scale, which is precisely determined by Planck. Local direct measurements of the Hubble parameter H_0 have shown that this value is larger than the one calculated at early times, a tension that has recently grown to 5σ . In order to help alleviate the tension, we propose a model which can deliver

extra relativistic degrees of freedom at CMB times while respecting BBN bounds on $\Delta N_{\rm eff}$. Our analysis is based on a two-sector model, one visible and the other hidden, where we assume a negligible particle abundance of the hidden sector particles in the early universe, and where the hidden sector particles are generated by the out-of-equilibrium annihilation of SM particles into particles in the hidden sector. Because of that, the two sectors reside in heat baths at different temperatures with the hidden sector at a lower temperature than the visible sector. Thus our analysis uses a set of coupled Boltzmann equations which depend on temperatures of both the visible and the hidden sectors and involves correlated temperature evolution of both sectors. In this set up we show that for a range of kinetic mixing and dark photon mass consistent with experimental limits, the visible and the dark sectors do not thermalize which implies that the dark sector particles never reach their equilibrium number densities. However, their phase space distributions can still be described by a Maxwell-Boltzmann distribution since they achieve chemical and kinetic equilibrium during the dark sector thermal history. The fact that the dark particles, especially the relativistic particle ϕ , never reach their equilibrium distribution allows to evade the constraint on $\Delta N_{\rm eff}^{\rm BBN}$. With a specific choice of couplings, late decays of $S \to \phi \phi$ can contribute the right amount to $\Delta N_{\rm eff}^{\rm CMB}$ thus resolving the Hubble tension. The model we present is cosmologically consistent since the formalism allows for correlated evolution of the temperatures of the hidden and the visible sectors which are not in thermal equilibrium. In fact it is the lack of thermal equilibrium between the hidden and visible sectors which forces consistency with the BBN constraint while allowing the enhancement of $N_{
m eff}$ at CMB time. However, as noted earlier, while $\Delta N_{\rm eff}$ at recombination time would weaken the Hubble tension, a better understanding of how this affects the CMB power spectrum requires a fit of the cosmological parameters to the CMB data.

Acknowledgments

The research of AA and MK was supported by the BMBF under contract 05P21PMCAA and by the DFG through the Research Training Network 2149 "Strong and Weak Interactions — from Hadrons to Dark Matter", while the research of PN was supported in part by the NSF Grant PHY-1913328.

9 Further details of the analysis

In this appendix we give further details of the analysis presented in the main body of the paper. In appendix A we give the formulae for the effective energy and entropy degrees of freedom, in appendix B we give details of mixings of the two U(1) sectors and in appendix C we give the Boltzmann equations with visible and hidden sector temperatures.

A Degrees of freedom

Here we focus on the hidden sector energy effective energy degrees of freedom g_{eff}^h in eq. (3.4) and on the hidden sector entropy effective degrees of freedom h_{eff}^h in eq. (3.1). They include degrees of freedom for the dark photon, the dark fermion and the scalars S and ϕ so that

$$g_{\text{eff}}^{h} = g_{\text{eff}}^{\gamma'} + \frac{7}{8}g_{\text{eff}}^{D} + g_{\phi} + g_{S}, \text{ and } h_{\text{eff}}^{h} = h_{\text{eff}}^{\gamma'} + \frac{7}{8}h_{\text{eff}}^{D} + h_{\phi} + h_{S},$$
 (A.1)

where $g_{\phi} = g_S = h_{\phi} = h_S = 1$ and at temperature T_h , g_{eff} and h_{eff} for the particles γ' and D are given by [71]

$$g_{\text{eff}}^{\gamma'} = \frac{45}{\pi^4} \int_{x_{\gamma'}}^{\infty} \frac{\sqrt{x^2 - x_{\gamma'}^2}}{e^x - 1} x^2 dx, \quad \text{and} \quad h_{\text{eff}}^{\gamma'} = \frac{45}{4\pi^4} \int_{x_{\gamma'}}^{\infty} \frac{\sqrt{x^2 - x_{\gamma'}^2}}{e^x - 1} (4x^2 - x_{\gamma'}^2) dx,$$

$$g_{\text{eff}}^D = \frac{60}{\pi^4} \int_{x_D}^{\infty} \frac{\sqrt{x^2 - x_D^2}}{e^x + 1} x^2 dx, \quad \text{and} \quad h_{\text{eff}}^D = \frac{15}{\pi^4} \int_{x_D}^{\infty} \frac{\sqrt{x^2 - x_D^2}}{e^x + 1} (4x^2 - x_D^2) dx.$$
(A.2)

Here $x_{\gamma'}$ and x_D are defined so that $x_{\gamma'} = m_{\gamma'}/T_h$ and $x_D = m_D/T_h$. The limit $x_{\gamma'} \to 0$ gives $g_{\rm eff}^{D'} = h_{\rm eff}^{\gamma'} \to 3$ and the limit $x_D \to 0$ gives $g_{\rm eff}^D = h_{\rm eff}^D \to 4$. Further details of the model are given in appendix B.

B Model details

In this appendix we give further details of the extended model with an additional $U(1)_X$ gauge group factor beyond the SM gauge group. In addition to the electroweak SM gauge fields A_a^μ (a=1–3) of $SU(2)_L$ and B_μ of $U(1)_Y$, we have a $U(1)_X$ gauge field C_μ . The mixing of the gauge fields in the neutral sector leads to a 3×3 mass square matrix whose diagonalization leads to the photon, the Z boson and a new massive neutral field which we label as the dark photon. Here we display the form of the couplings that enter $\Delta \mathcal{L}^{\text{int}}$. Thus the couplings g_Z^D, g_Y^D and $g_{\gamma'}^D$ that appear in $\Delta \mathcal{L}^{\text{int}}$ (see eq. (2.4)) are given by

$$g_Z^D = g_X Q_X (\mathcal{R}_{12} - s_\delta \mathcal{R}_{22}), \quad g_\gamma^D = g_X Q_X (\mathcal{R}_{13} - s_\delta \mathcal{R}_{23}), \quad g_{\gamma'}^D = g_X Q_X (\mathcal{R}_{11} - s_\delta \mathcal{R}_{21}),$$
(B.1)

where the matrix \mathcal{R} is given by eq. (23) of [25]. It involves three Euler angles (θ, ϕ, ψ) which diagonalize the Stueckelberg mass matrix such that $\mathcal{R}^T \mathcal{M}^2 \mathcal{R} = \text{diag}(m_{\gamma'}^2, m_Z^2, 0)$, where \mathcal{M}^2 is defined by eq. (21) of [25]. The angles ϕ, θ, ψ are defined as

$$\tan \phi = -s_{\delta}, \quad \tan \theta = \frac{g_Y}{g_2} c_{\delta} \cos \phi, \quad \tan 2\psi = \frac{2\bar{\epsilon} m_Z^2 \sin \theta}{m_{\gamma'}^2 - m_Z^2 + (m_{\gamma'}^2 + m_Z^2 - m_W^2)\bar{\epsilon}^2}, \quad (B.2)$$

where $s_{\delta} = \sinh \delta$ and $c_{\delta} = \cosh \delta$.

C Boltzmann equations with visible and hidden sector temperatures

Since, in general, the visible and the hidden sector reside in different temperature baths, the Boltzmann equations for the yields Y_D , $Y_{\gamma'}$, Y_{ϕ} and Y_S involve these two temperatures and are given by

$$\begin{split} \frac{dY_{\phi}}{dT_{h}} &= -\frac{\mathfrak{s}}{H} \left(\frac{d\rho_{h}/dT_{h}}{4\zeta\rho_{h} - j_{h}/H} \right) \left[\frac{1}{2} \langle \sigma v \rangle_{D\bar{D} \rightarrow \phi\gamma'} (T_{h}) \left(Y_{D}^{2} - Y_{D}^{\text{eq}}(T_{h})^{2} \frac{Y_{\phi}Y_{\gamma'}}{Y_{\phi}^{\text{eq}}(T_{h})Y_{\gamma'}^{\text{eq}}(T_{h})} \right) \right. \\ & + \frac{1}{2} \langle \sigma v \rangle_{D\bar{D} \rightarrow \phi S} (T_{h}) \left(Y_{D}^{2} - Y_{D}^{\text{eq}}(T_{h})^{2} \frac{Y_{\phi}Y_{S}}{Y_{\phi}^{\text{eq}}(T_{h})Y_{S}^{\text{eq}}(T_{h})} \right) \\ & + \frac{1}{2} \langle \sigma v \rangle_{D\bar{D} \rightarrow \phi\phi} (T_{h}) \left(Y_{D}^{2} - Y_{D}^{\text{eq}}(T_{h})^{2} \frac{Y_{\phi}^{2}}{Y_{\phi}^{\text{eq}}(T_{h})^{2}} \right) \end{split}$$

$$\begin{split} &-\langle\sigma v\rangle_{\phi\phi\to SS}(T_h)\left(Y_\phi^2-Y_\phi^{\rm eq}(T_h)^2\frac{Y_S^2}{Y_S^{\rm eq}(T_h)^2}\right)\\ &-\langle\sigma v\rangle_{\phi\phi\to S}(T_h)\left(Y_\phi^2-Y_\phi^{\rm eq}(T_h)^2\frac{Y_S}{Y_S^{\rm eq}(T_h)}\right)\right], \qquad (\text{C.1})\\ \frac{dY_S}{dT_h} &= -\frac{s}{H}\left(\frac{d\rho_h/dT_h}{4\zeta\rho_h-j_h/H}\right)\left[\frac{1}{2}\langle\sigma v\rangle_{D\bar{D}\to S\gamma'}(T_h)\left(Y_D^2-Y_D^{\rm eq}(T_h)^2\frac{Y_S}{Y_S^{\rm eq}(T_h)}\right)\right], \qquad (\text{C.1})\\ &+\frac{1}{2}\langle\sigma v\rangle_{D\bar{D}\to \phi S}(T_h)\left(Y_D^2-Y_D^{\rm eq}(T_h)^2\frac{Y_SY_{\gamma'}}{Y_S^{\rm eq}(T_h)Y_{\gamma'}^{\rm eq}(T_h)}\right)\\ &+\frac{1}{2}\langle\sigma v\rangle_{D\bar{D}\to SS}(T_h)\left(Y_D^2-Y_D^{\rm eq}(T_h)^2\frac{Y_S^2}{Y_S^{\rm eq}(T_h)Y_S^{\rm eq}(T_h)}\right)\\ &+\frac{1}{2}\langle\sigma v\rangle_{D\bar{D}\to SS}(T_h)\left(Y_\phi^2-Y_\phi^{\rm eq}(T_h)^2\frac{Y_S^2}{Y_S^{\rm eq}(T_h)^2}\right)\\ &+\langle\sigma v\rangle_{\phi\phi\to SS}(T_h)\left(Y_\phi^2-Y_\phi^{\rm eq}(T_h)^2\frac{Y_S^2}{Y_S^{\rm eq}(T_h)}\right)\right], \qquad (\text{C.2})\\ \frac{dY_{\gamma'}}{dT_h} &= -\frac{s}{H}\left(\frac{d\rho_h/dT_h}{4\zeta\rho_h-j_h/H}\right)\left[-\langle\sigma v\rangle_{\gamma'\gamma'\to D\bar{D}}(T_h)\left(Y_\gamma^2-Y_\phi^{\rm eq}(T_h)^2\frac{Y_S^2}{Y_S^{\rm eq}(T_h)}\right)\right]\\ &+\frac{1}{2}\langle\sigma v\rangle_{D\bar{D}\to \phi\gamma'}(T_h)\left(Y_D^2-Y_D^{\rm eq}(T_h)^2\frac{Y_S^2}{Y_S^{\rm eq}(T_h)Y_\gamma^{\rm eq}(T_h)}\right)\\ &+\frac{1}{2}\langle\sigma v\rangle_{D\bar{D}\to S\gamma'}(T_h)\left(Y_D^2-Y_D^{\rm eq}(T_h)^2\frac{Y_S^2}{Y_S^{\rm eq}(T_h)Y_\gamma^{\rm eq}(T_h)}\right)\\ &-\frac{1}{s}\langle\Gamma_{\gamma'\to D\bar{D}}\rangle\langle T_h\rangle\left(Y_\gamma^2-Y_\gamma^{\rm eq}(T_h)\frac{Y_\gamma^2}{Y_\rho^{\rm eq}(T_h)Y_\gamma^{\rm eq}(T_h)}\right)\\ &-\frac{1}{2}\langle\sigma v\rangle_{D\bar{D}\to \gamma'\gamma'}(T_h)\left(Y_D^2-Y_D^{\rm eq}(T_h)^2\frac{Y_\gamma^2}{Y_\rho^{\rm eq}(T_h)^2}\right)\\ &-\frac{1}{2}\langle\sigma v\rangle_{D\bar{D}\to \phi\phi'}(T_h)\left(Y_D^2-Y_D^{\rm eq}(T_h)^2\frac{Y_\gamma^2}{Y_\rho^{\rm eq}(T_h)^2}\right)\\ &-\frac{1}{2}\langle\sigma v\rangle_{D\bar{D}\to$$

$$-\frac{1}{2}\langle \sigma v \rangle_{D\bar{D}\to S\gamma'}(T_h) \left(Y_D^2 - Y_D^{\text{eq}}(T_h)^2 \frac{Y_S Y_{\gamma'}}{Y_S^{\text{eq}}(T_h) Y_{\gamma'}^{\text{eq}}(T_h)} \right)$$
$$-\frac{1}{2}\langle \sigma v \rangle_{D\bar{D}\to S\phi}(T_h) \left(Y_D^2 - Y_D^{\text{eq}}(T_h)^2 \frac{Y_S Y_{\phi}}{Y_S^{\text{eq}}(T_h) Y_{\phi}^{\text{eq}}(T_h)} \right)$$
$$-\frac{1}{2}\langle \sigma v \rangle_{D\bar{D}\to \gamma'}(T_h) Y_D^2 + \frac{1}{s}\langle \Gamma_{\gamma'\to D\bar{D}}\rangle(T_h) Y_{\gamma'} \right]. \tag{C.4}$$

The thermally averaged cross sections appearing in eqs. (C.1)–(C.4) are given by

$$\langle \sigma v \rangle_{a\bar{a} \to bc}(T) = \frac{1}{8m_a^4 T K_2^2(m_a/T)} \int_{4m_a^2}^{\infty} ds \ \sigma(s) \sqrt{s} \left(s - 4m_a^2\right) K_1(\sqrt{s}/T), \tag{C.5}$$

and

$$n_i^{\rm eq}(T)^2 \langle \sigma v \rangle_{i\bar{i} \to \gamma'}(T) = \frac{T}{32\pi^4} \int_{s_0}^{\infty} ds \ \sigma(s) \sqrt{s} \left(s - s_0\right) K_1(\sqrt{s}/T),\tag{C.6}$$

where K_1 is the modified Bessel function of the second kind and degree one and s_0 is the minimum of the Mandelstam variable s. Note the appearance of the prefactor $\frac{s}{H} \left(\frac{d\rho_h/dT_h}{4\zeta\rho_h-j_h/H} \right)$ in the Boltzmann equations which has a dependence on the source j_h .

The equilibrium yield is given by

$$Y_i^{\text{eq}} = \frac{n_i^{\text{eq}}}{g} = \frac{g_i}{2\pi^2 g} m_i^2 T K_2(m_i/T),$$
 (C.7)

where n_i is the number density of a SM particle species i, g_i is its number of degrees of freedom, and m_i its mass. Further, K_2 is the modified Bessel function of the second kind and degree two and the J functions in eq. (3.7) are given by

$$n_i^{\rm eq}(T)^2 J(i \ \bar{i} \to D\bar{D})(T) = \frac{T}{32\pi^4} \int_{s_0}^{\infty} ds \ \sigma_{D\bar{D} \to i\bar{i}} \bar{s}(s-s_0) K_2(\sqrt{s}/T),$$
 (C.8)

$$n_i^{\rm eq}(T)^2 J(i \ \bar{i} \to \gamma')(T) = \frac{T}{32\pi^4} \int_{s_0}^{\infty} ds \ \sigma_{i\bar{i}\to\gamma'} s(s-s_0) K_2(\sqrt{s}/T), \tag{C.9}$$

$$n_{\gamma'}J(\gamma' \to f\bar{f})(T_h) = n_{\gamma'}m_{\gamma'}\Gamma_{\gamma' \to f\bar{f}},$$
 (C.10)

$$J(ab \to cd)(T_h) = \frac{1}{8T_h m_a^2 m_b^2 K_2(m_a/T_h) K_2(m_b/T_h)} \times \int_{(m_a + m_b)^2}^{\infty} ds \ \sigma_{ab \to cd}(s) s[s - (m_a + m_b)^2] K_2(\sqrt{s}/T_h).$$
(C.11)

We note in passing that in eq. (C.3) the processes $i \ \bar{i} \to \gamma' \gamma, \gamma' Z, \gamma' \gamma'$ also contribute. However, their contributions are relatively small compared to those of $i \ \bar{i} \to \gamma'$.

References

- [1] A.G. Riess et al., A Comprehensive Measurement of the Local Value of the Hubble Constant with 1 km/s/Mpc Uncertainty from the Hubble Space Telescope and the SH0ES Team, arXiv:2112.04510 [INSPIRE].
- [2] Planck collaboration, Planck 2018 results. Part VI. Cosmological parameters, Astron. Astrophys. 641 (2020) A6 [Erratum ibid. 652 (2021) C4] [arXiv:1807.06209] [INSPIRE].

- [3] E. Di Valentino et al., In the realm of the Hubble tension a review of solutions, Class. Quant. Grav. 38 (2021) 153001 [arXiv:2103.01183] [INSPIRE].
- [4] R. Solomon, G. Agarwal and D. Stojkovic, Environment Dependent Electron Mass and the H₀-Tension, arXiv: 2201.03127 [INSPIRE].
- [5] E. Fernandez-Martinez, M. Pierre, E. Pinsard and S. Rosauro-Alcaraz, Inverse Seesaw, dark matter and the Hubble tension, Eur. Phys. J. C 81 (2021) 954 [arXiv:2106.05298] [INSPIRE].
- [6] M. Escudero and S.J. Witte, The hubble tension as a hint of leptogenesis and neutrino mass generation, Eur. Phys. J. C 81 (2021) 515 [arXiv:2103.03249] [INSPIRE].
- [7] J. Gehrlein and M. Pierre, A testable hidden-sector model for Dark Matter and neutrino masses, JHEP 02 (2020) 068 [arXiv:1912.06661] [INSPIRE].
- [8] M. Escudero, D. Hooper, G. Krnjaic and M. Pierre, Cosmology with A Very Light $L_{\mu} L_{\tau}$ Gauge Boson, JHEP 03 (2019) 071 [arXiv:1901.02010] [INSPIRE].
- [9] R.H. Cyburt, B.D. Fields, K.A. Olive and T.-H. Yeh, Big Bang Nucleosynthesis: 2015, Rev. Mod. Phys. 88 (2016) 015004 [arXiv:1505.01076] [INSPIRE].
- [10] C. Pitrou, A. Coc, J.-P. Uzan and E. Vangioni, Precision big bang nucleosynthesis with improved Helium-4 predictions, Phys. Rept. 754 (2018) 1 [arXiv:1801.08023] [INSPIRE].
- [11] G. Mangano, G. Miele, S. Pastor, T. Pinto, O. Pisanti and P.D. Serpico, Relic neutrino decoupling including flavor oscillations, Nucl. Phys. B 729 (2005) 221 [hep-ph/0506164] [INSPIRE].
- [12] A.G. Riess et al., New Parallaxes of Galactic Cepheids from Spatially Scanning the Hubble Space Telescope: Implications for the Hubble Constant, Astrophys. J. 855 (2018) 136 [arXiv:1801.01120] [INSPIRE].
- [13] A.G. Riess, S. Casertano, W. Yuan, L.M. Macri and D. Scolnic, Large Magellanic Cloud Cepheid Standards Provide a 1% Foundation for the Determination of the Hubble Constant and Stronger Evidence for Physics beyond ΛCDM, Astrophys. J. 876 (2019) 85 [arXiv:1903.07603] [INSPIRE].
- [14] Pan-STARRS1 collaboration, The Complete Light-curve Sample of Spectroscopically Confirmed SNe Ia from Pan-STARRS1 and Cosmological Constraints from the Combined Pantheon Sample, Astrophys. J. 859 (2018) 101 [arXiv:1710.00845] [INSPIRE].
- [15] O. Seto and Y. Toda, Comparing early dark energy and extra radiation solutions to the Hubble tension with BBN, Phys. Rev. D 103 (2021) 123501 [arXiv:2101.03740] [INSPIRE].
- [16] O. Seto and Y. Toda, Hubble tension in lepton asymmetric cosmology with an extra radiation, Phys. Rev. D 104 (2021) 063019 [arXiv:2104.04381] [INSPIRE].
- [17] S. Vagnozzi, New physics in light of the H₀ tension: An alternative view, Phys. Rev. D 102 (2020) 023518 [arXiv:1907.07569] [INSPIRE].
- [18] M.G. Dainotti, B. De Simone, T. Schiavone, G. Montani, E. Rinaldi and G. Lambiase, On the Hubble constant tension in the SNe Ia Pantheon sample, Astrophys. J. 912 (2021) 150 [arXiv:2103.02117] [INSPIRE].
- [19] M.G. Dainotti et al., On the Evolution of the Hubble Constant with the SNe Ia Pantheon Sample and Baryon Acoustic Oscillations: A Feasibility Study for GRB-Cosmology in 2030, Galaxies 10 (2022) 24 [arXiv:2201.09848] [INSPIRE].
- [20] B. Holdom, Two U(1)'s and Epsilon Charge Shifts, Phys. Lett. B 166 (1986) 196 [INSPIRE].
- [21] B. Holdom, Oblique electroweak corrections and an extra gauge boson, Phys. Lett. B 259 (1991) 329 [INSPIRE].
- [22] B. Körs and P. Nath, A Stueckelberg extension of the standard model, Phys. Lett. B 586 (2004) 366 [hep-ph/0402047] [INSPIRE].

- [23] B. Körs and P. Nath, A Supersymmetric Stueckelberg U(1) extension of the MSSM, JHEP 12 (2004) 005 [hep-ph/0406167] [INSPIRE].
- [24] K. Cheung and T.-C. Yuan, Hidden fermion as milli-charged dark matter in Stueckelberg Z' model, JHEP 03 (2007) 120 [hep-ph/0701107] [INSPIRE].
- [25] D. Feldman, Z. Liu and P. Nath, The Stueckelberg Z' Extension with Kinetic Mixing and Milli-Charged Dark Matter From the Hidden Sector, Phys. Rev. D 75 (2007) 115001 [hep-ph/0702123] [INSPIRE].
- [26] A. Aboubrahim, W.-Z. Feng, P. Nath and Z.-Y. Wang, Self-interacting hidden sector dark matter, small scale galaxy structure anomalies, and a dark force, Phys. Rev. D 103 (2021) 075014 [arXiv:2008.00529] [INSPIRE].
- [27] A. Aboubrahim, T. Ibrahim, M. Klasen and P. Nath, A decaying neutralino as dark matter and its gamma ray spectrum, Eur. Phys. J. C 81 (2021) 680 [arXiv:2012.10795] [INSPIRE].
- [28] A. Aboubrahim, W.-Z. Feng, P. Nath and Z.-Y. Wang, A multi-temperature universe can allow a sub-MeV dark photon dark matter, JHEP 06 (2021) 086 [arXiv:2103.15769] [INSPIRE].
- [29] A. Aboubrahim, P. Nath and Z.-Y. Wang, A cosmologically consistent millicharged dark matter solution to the EDGES anomaly of possible string theory origin, JHEP 12 (2021) 148 [arXiv:2108.05819] [INSPIRE].
- [30] A. Aboubrahim, W.-Z. Feng, P. Nath and Z.-Y. Wang, Hidden sectors and a multi-temperature universe, in proceedings of the 2022 Snowmass Summer Study, Seattle, WA, U.S.A., 17–26 July 2022, arXiv:2106.06494 [INSPIRE].
- [31] R. Foot and S. Vagnozzi, Dissipative hidden sector dark matter, Phys. Rev. D 91 (2015) 023512 [arXiv:1409.7174] [INSPIRE].
- [32] R. Foot and S. Vagnozzi, Solving the small-scale structure puzzles with dissipative dark matter, JCAP 07 (2016) 013 [arXiv:1602.02467] [INSPIRE].
- [33] M. Drees, F. Hajkarim and E.R. Schmitz, The Effects of QCD Equation of State on the Relic Density of WIMP Dark Matter, JCAP 06 (2015) 025 [arXiv:1503.03513] [INSPIRE].
- [34] PLANCK collaboration, Planck 2018 results. Part VI. Cosmological parameters, Astron. Astrophys. 641 (2020) A6 [Erratum ibid. 652 (2021) C4] [arXiv:1807.06209] [INSPIRE].
- [35] T. Binder, T. Bringmann, M. Gustafsson and A. Hryczuk, Early kinetic decoupling of dark matter: when the standard way of calculating the thermal relic density fails, Phys. Rev. D 96 (2017) 115010 [Erratum ibid. 101 (2020) 099901] [arXiv:1706.07433] [INSPIRE].
- [36] T. Binder, T. Bringmann, M. Gustafsson and A. Hryczuk, Dark matter relic abundance beyond kinetic equilibrium, Eur. Phys. J. C 81 (2021) 577 [arXiv:2103.01944] [INSPIRE].
- [37] T. Bringmann, Particle Models and the Small-Scale Structure of Dark Matter, New J. Phys. 11 (2009) 105027 [arXiv:0903.0189] [INSPIRE].
- [38] T. Bringmann and S. Hofmann, Thermal decoupling of WIMPs from first principles, JCAP 04 (2007) 016 [Erratum JCAP 03 (2016) E02] [hep-ph/0612238] [INSPIRE].
- [39] P. Gondolo, J. Hisano and K. Kadota, The Effect of quark interactions on dark matter kinetic decoupling and the mass of the smallest dark halos, Phys. Rev. D 86 (2012) 083523 [arXiv:1205.1914] [INSPIRE].
- [40] T. Bringmann, H.T. Ihle, J. Kersten and P. Walia, Suppressing structure formation at dwarf galaxy scales and below: late kinetic decoupling as a compelling alternative to warm dark matter, Phys. Rev. D 94 (2016) 103529 [arXiv:1603.04884] [INSPIRE].
- [41] CHARM collaboration, Search for Axion Like Particle Production in 400 GeV Proton-Copper Interactions, Phys. Lett. B 157 (1985) 458 [INSPIRE].

- [42] Y.-D. Tsai, P. de Niverville and M.X. Liu, Dark Photon and Muon g 2 Inspired Inelastic Dark Matter Models at the High-Energy Intensity Frontier, Phys. Rev. Lett. 126 (2021) 181801 [arXiv:1908.07525] [INSPIRE].
- [43] E.M. Riordan et al., A Search for Short Lived Axions in an Electron Beam Dump Experiment, Phys. Rev. Lett. 59 (1987) 755 [INSPIRE].
- [44] J. Blumlein et al., Limits on neutral light scalar and pseudoscalar particles in a proton beam dump experiment, Z. Phys. C 51 (1991) 341 [INSPIRE].
- [45] J. Blumlein et al., Limits on the mass of light (pseudo)scalar particles from Bethe-Heitler e⁺e⁻ and μ⁺μ⁻ pair production in a proton-iron beam dump experiment, Int. J. Mod. Phys. A 7 (1992) 3835 [INSPIRE].
- [46] J. Blümlein and J. Brunner, New Exclusion Limits on Dark Gauge Forces from Proton Bremsstrahlung in Beam-Dump Data, Phys. Lett. B 731 (2014) 320 [arXiv:1311.3870] [INSPIRE].
- [47] J. Blumlein and J. Brunner, New Exclusion Limits for Dark Gauge Forces from Beam-Dump Data, Phys. Lett. B 701 (2011) 155 [arXiv:1104.2747] [INSPIRE].
- [48] S. Andreas, C. Niebuhr and A. Ringwald, New Limits on Hidden Photons from Past Electron Beam Dumps, Phys. Rev. D 86 (2012) 095019 [arXiv:1209.6083] [INSPIRE].
- [49] J.D. Bjorken, R. Essig, P. Schuster and N. Toro, New Fixed-Target Experiments to Search for Dark Gauge Forces, Phys. Rev. D 80 (2009) 075018 [arXiv:0906.0580] [INSPIRE].
- [50] M. Endo, K. Hamaguchi and G. Mishima, Constraints on Hidden Photon Models from Electron g-2 and Hydrogen Spectroscopy, Phys. Rev. D 86 (2012) 095029 [arXiv:1209.2558] [INSPIRE].
- [51] BABAR collaboration, Search for a Dark Photon in e⁺e⁻ Collisions at BaBar, Phys. Rev. Lett. 113 (2014) 201801 [arXiv:1406.2980] [INSPIRE].
- [52] NA48/2 collaboration, Search for the dark photon in π^0 decays, Phys. Lett. B **746** (2015) 178 [arXiv:1504.00607] [INSPIRE].
- [53] NA64 collaboration, Search for a Hypothetical 16.7 MeV Gauge Boson and Dark Photons in the NA64 Experiment at CERN, Phys. Rev. Lett. 120 (2018) 231802 [arXiv:1803.07748] [INSPIRE].
- [54] NA64 collaboration, Improved limits on a hypothetical X(16.7) boson and a dark photon decaying into e⁺e⁻ pairs, Phys. Rev. D 101 (2020) 071101 [arXiv:1912.11389] [INSPIRE].
- [55] LHCb collaboration, Search for Dark Photons Produced in 13 TeV pp Collisions, Phys. Rev. Lett. 120 (2018) 061801 [arXiv:1710.02867] [INSPIRE].
- [56] LHCb collaboration, Search for $A' \rightarrow \mu^+\mu^-$ Decays, Phys. Rev. Lett. 124 (2020) 041801 [arXiv:1910.06926] [INSPIRE].
- [57] P. Ilten, Y. Soreq, M. Williams and W. Xue, Serendipity in dark photon searches, JHEP 06 (2018) 004 [arXiv:1801.04847] [INSPIRE].
- [58] J.H. Chang, R. Essig and S.D. McDermott, Revisiting Supernova 1987A Constraints on Dark Photons, JHEP 01 (2017) 107 [arXiv:1611.03864] [INSPIRE].
- [59] P.F. de Salas and S. Pastor, Relic neutrino decoupling with flavour oscillations revisited, JCAP 07 (2016) 051 [arXiv:1606.06986] [INSPIRE].
- [60] S. Bashinsky and U. Seljak, Neutrino perturbations in CMB anisotropy and matter clustering, Phys. Rev. D 69 (2004) 083002 [astro-ph/0310198] [INSPIRE].
- [61] Z. Hou, R. Keisler, L. Knox, M. Millea and C. Reichardt, How Massless Neutrinos Affect the Cosmic Microwave Background Damping Tail, Phys. Rev. D 87 (2013) 083008 [arXiv:1104.2333] [INSPIRE].

- [62] D. Baumann, D. Green, J. Meyers and B. Wallisch, Phases of New Physics in the CMB, JCAP 01 (2016) 007 [arXiv:1508.06342] [INSPIRE].
- [63] A. Friedland, K.M. Zurek and S. Bashinsky, Constraining Models of Neutrino Mass and Neutrino Interactions with the Planck Satellite, arXiv:0704.3271 [INSPIRE].
- [64] B. Follin, L. Knox, M. Millea and Z. Pan, First Detection of the Acoustic Oscillation Phase Shift Expected from the Cosmic Neutrino Background, Phys. Rev. Lett. 115 (2015) 091301 [arXiv:1503.07863] [INSPIRE].
- [65] N. Blinov and G. Marques-Tavares, Interacting radiation after Planck and its implications for the Hubble Tension, JCAP 09 (2020) 029 [arXiv:2003.08387] [INSPIRE].
- [66] A. Berlin and N. Blinov, *Thermal Dark Matter Below an MeV*, *Phys. Rev. Lett.* **120** (2018) 021801 [arXiv:1706.07046] [INSPIRE].
- [67] Z. Chacko, L.J. Hall, T. Okui and S.J. Oliver, CMB signals of neutrino mass generation, Phys. Rev. D 70 (2004) 085008 [hep-ph/0312267] [INSPIRE].
- [68] Z. Chacko, L.J. Hall, S.J. Oliver and M. Perelstein, Late time neutrino masses, the LSND experiment and the cosmic microwave background, Phys. Rev. Lett. 94 (2005) 111801 [hep-ph/0405067] [INSPIRE].
- [69] M. Escudero Abenza, Precision early universe thermodynamics made simple: N_{eff} and neutrino decoupling in the Standard Model and beyond, JCAP 05 (2020) 048 [arXiv:2001.04466] [INSPIRE].
- [70] W. Hu, M. Fukugita, M. Zaldarriaga and M. Tegmark, CMB observables and their cosmological implications, Astrophys. J. 549 (2001) 669 [astro-ph/0006436] [INSPIRE].
- [71] M. Hindmarsh and O. Philipsen, WIMP dark matter and the QCD equation of state, Phys. Rev. D 71 (2005) 087302 [hep-ph/0501232] [INSPIRE].